Dalton Transactions

ROYAL SOCIETY OF CHEMISTRY

PAPER

View Article Online
View Journal | View Issue



Cite this: *Dalton Trans.*, 2025, **54**, 10128

# Evaluation of relaxation dynamics from excited states of $Ho^{3+}$ ions in sol–gel nano-glass-ceramic materials†

Natalia Pawlik, *[a] Joanna Śmiarowska,[a] Bartosz Handke,[b] Maciej Zubko,[c,d] Maciej Sitarz[b] and Wojciech A. Pisarski[a]

In this paper, a series of oxyfluoride $SiO_2$-$LaF_3$ nano-glass-ceramics (GCs) activated by $Ho^{3+}$ ions with variable concentrations were synthesized by the sol–gel method. The crystallization of the $LaF_3$ fluoride phase for all prepared series was verified by XRD measurements and TEM microscopy. For the fabricated GCs, a series of specific luminescence bands within VIS, NIR, and MIR regions were recorded, and the most prominent emissions were assigned to the following $4f^{10}$–$4f^{10}$ transitions of $Ho^{3+}$ ions: $(^5S_2,^5F_4) \rightarrow {}^5I_8$ (green), $^5F_5 \rightarrow {}^5I_8$ (red), $^5I_6 \rightarrow {}^5I_8$ (NIR, ~1.19 μm), and $^5I_7 \rightarrow {}^5I_8$ (MIR, ~2.0 μm). Based on the mutual intensities of recorded individual emission bands, their percentage contributions ($\beta$) were evaluated. It was found that the calculated values of $\beta$ coefficients are strongly dependent on the applied annealing temperature (700 or 900 °C), the average size of precipitated $LaF_3$ crystals, and the concentration of $Ho^{3+}$ ions. Thus, the results indicate that the connotation in the mutual population of the individual excited states (*i.e.*, $(^5S_2,^5F_4)$, $^5F_5$, $^5I_6$, and $^5I_7$) – correlated with the relaxation dynamics from the above-mentioned levels – relies on the phonon energy (modified during an increase in annealing temperature (700 °C → 900 °C)) in the nearest proximity around $Ho^{3+}$ ions by activating (or suspending) the non-radiative multiphonon channels (MPR). The performed luminescence studies tentatively showed that increasing the heat-treatment temperature favors $Ho^{3+}$ migration from the silicate network into the low-oscillation energy $LaF_3$ phase, unfavoring the non-radiative MPR processes between the $(^5S_2,^5F_4)$ and the $^5F_5$ states, and also between the excited $^5I_6/^5I_7$ states and the $^5I_8$ ground level. The prepared $Ho^{3+}$-doped GCs are able to emit green light with high color purity (CP) reaching even 98%, and generate long-lived NIR/MIR emissions at ~1.19 μm (up to $\tau(^5I_6)$ = 10.19 ms) and ~2.0 μm (up to $\tau(^5I_7)$ = 8.44 ms), which could predispose them for use in optoelectronic devices.

Received 12th February 2025,
Accepted 22nd May 2025

DOI: 10.1039/d5dt00342c

rsc.li/dalton



## Introduction

Trivalent lanthanide ions – exhibiting a specific electron configuration, *i.e.*, $[Xe]4f^n$ ($n$ = 0–14) – are characterized by multiple energy states within a broad range of electromagnetic spectra from ultraviolet (UV), through visible (VIS) up to near- or mid-infrared (NIR/MIR) irradiation.[1] Among them, $Ho^{3+}$ ions with a $[Xe]4f^{10}$ configuration emit green ($(^5S_2,^5F_4) \rightarrow {}^5I_8$) and red ($^5F_5 \rightarrow {}^5I_8$) light, as well as radiation from NIR and MIR ranges, *i.e.*, 1.2 μm ($^5I_6 \rightarrow {}^5I_8$), 1.38 μm ($(^5S_2,^5F_4) \rightarrow {}^5I_5$), 1.5 μm ($^5F_5 \rightarrow {}^5I_6$), 2.0 μm ($^5I_7 \rightarrow {}^5I_8$), and even 3.9 μm.[2–4] The unique properties of $Ho^{3+}$ ions are strictly correlated with their multiple *meta*-stable levels; those luminescence peculiarities open diverse application possibilities.[5] Indeed, $Ho^{3+}$-doped materials are mainly dedicated to green lighting applications (*e.g.*, for lasers or color displays), as was demonstrated for plentiful glassy hosts,[2,6–9] and also for several types of ceramic materials (for example, $Y_2O_3$ or $MTiO_3$ (M = Ca or Ba)).[10–12] Additionally, the literature mentions the possibility of dominant generation of red luminescence, as was found for glass ceramics containing $BaAlBO_3F_2$:$Ho^{3+}$ nanocrystals or $Ho^{3+}$-doped fibers.[13,14] Interestingly, as was described for glass-ceramics containing $Ba_4Y_3F_{12}$:$Yb^{3+}$/$Ho^{3+}$ nanoparticles, co-doping with $Ce^{3+}$ favors the occurrence of appropriate cross-relaxation (CR) processes, responsible for the gradual depopulation of the upper-lying $(^5S_2,^5F_4)$ levels with a simultaneous enhance-

[a]*University of Silesia, Institute of Chemistry, 9 Szkolna Str., 40-007 Katowice, Poland. E-mail: natalia.pawlik@us.edu.pl*
[b]*AGH University of Krakow, Faculty of Materials Science and Ceramics, 30 Mickiewicza Av., 30-059 Kraków, Poland*
[c]*University of Silesia, Institute of Materials Engineering, 75. Pułku Piechoty 1A Str., 41-500 Chorzów, Poland*
[d]*University of Hradec Králové, Department of Physics, Rokitanského 62, 50003 Hradec Králové, Czech Republic*
† Electronic supplementary information (ESI) available. See DOI: https://doi.org/10.1039/d5dt00342c

ment in the occupation of the lower-lying $^5F_5$ state, resulting in the generation of tunable green-to-red luminescence dependent on the $Ce^{3+}$ concentration.[15] It is expected that visible emission originating from $Ho^{3+}$ ions could be applied in data storage systems and sensors.[6,16,17] Moreover, $Ho^{3+}$ luminescence with a combination of blue-emitting centers (like $Tm^{3+}$) is suitable for producing illumination dedicated to technologies based on white-light emitting diodes (WLEDs), as was presented for $Ho^{3+}/Yb^{3+}/Tm^{3+}$ triply-doped $GeO_2$-$Nb_2O_5$ nanostructured materials.[18]

Even with the tremendous application of VIS luminescence from $Ho^{3+}$-doped optical materials, nonetheless, the potential utility area of NIR and MIR emissions has also attracted attention from many researchers. Factually, the characteristic NIR luminescence of $Ho^{3+}$ ions at 1.2 μm – located near the second telecommunication window – could be applied in designing O-band amplifiers, as was presented, *e.g.*, for heavy-metal gallate glasses.[19] Importantly, ~1.2 μm lasers can be applied in medicine or for oxygen detection, and this fact was first reported by NASA;[20] thus, optical fibers operating on the $^5I_6 \rightarrow {}^5I_8$ electronic transition of $Ho^{3+}$ may be suitable for lasing purposes as was described for $Ho^{3+}/Yb^{3+}$ co-doped $TeO_2$-$BaF_2$-$Y_2O_3$ glasses.[21] Furthermore, the 'eye-safe' MIR emission at 2.0 μm, imperceptible to the human eye, is utilized in remote sensing (LIDAR) devices, wind mapping, and laser ranger finders. Additionally, 2.0 μm wavelength is firmly absorbed by water molecules; thus, it could be used in surgery as an optical laser beam ensuring less damaged tissues, less bleeding, and limiting contamination in comparison with metallic ones; this MIR emission could find application not only in the detection of atmospheric pollutions, like greenhouse gases, *e.g.*, methane or carbon dioxide, but also in atmospheric communication systems.[3,22–25] The great fields of 2.0 μm wavelength utilities presented above are a strong motivation for designing and developing appropriate materials; factually, $Yb^{3+}/Ho^{3+}/Ce^{3+}$ triply-doped sodium-zinc-tellurite glasses,[26] $Er^{3+}/Ho^{3+}$ co-doped silicate glasses,[27] or $Yb^{3+}/Ho^{3+}$ co-doped oxyfluoride glass-ceramics[28] are considered as promising candidates for improving the $Ho^{3+}$ 2.0 μm fiber laser performance. Thus, considering the tremendous potential of $Ho^{3+}$-doped optical materials, their design and studies are essential for developing the current optoelectronics.

The intensities of the individual emission bands of $Ho^{3+}$ ions are sensitive to the oscillation energy in their local proximity in the host matrix.[16,29] Indeed, it is a well-known fact that multiphonon processes become more substantial if the energy gap is comparable with the phonon energy of the local neighborhood of $Ln^{3+}$.[24] Thus, the resultant intensities of individual luminescence bands of $Ho^{3+}$ strongly depend on the population of appropriate excited states, affected by the preferable location of dopant ions in the host matrix. Those connotations were described in detail for $Ho^{3+}/Yb^{3+}$ co-doped aluminosilicate glasses (G) and glass-ceramics containing $NaYF_4$ nanocrystals (GC).[30] Since the energy gap between the $^5I_6$ and $^5I_7$ levels of $Ho^{3+}$ ($\Delta E \approx 2550$ cm$^{-1}$) could be easily matched by two or three phonons of the glass host ($h\omega \approx 1100$ cm$^{-1}$), the authors established that the $^5I_6$ state could non-radiatively relax to the lower-lying $^5I_7$ level by a multiphonon-assisted process. Conversely, when $Ho^{3+}$ ions are preferentially located inside $NaYF_4$ nanocrystals with a lower oscillation energy ($h\omega \approx 324$ cm$^{-1}$), the multiphonon-assisted relaxation rate decreases greatly; thus, the upper-lying $^5I_6$ level is more occupied than the $^5I_7$ state. Resultantly, for glasses, $Ho^{3+}$ ions at the $^5I_7$ level can be efficiently populated to the upper $^5F_5$ state; therefore, the $^5F_5 \rightarrow {}^5I_8$ red emission dominates in emission spectra. In the case of glass-ceramics, $Ho^{3+}$ ions in the $^5I_6$ state can be mainly pumped into the ($^5S_2$,$^5F_4$) levels. Also, for $Ho^{3+}/Yb^{3+}$ co-doped glass-ceramics containing $CaF_2$ nanocrystals,[31] it was noticed that the correlation in mutual intensities of green ($^5S_2$,$^5F_4$) $\rightarrow {}^5I_8$) and red ($^5F_5 \rightarrow {}^5I_8$) emissions is closely associated with the local phonon energy around $Ho^{3+}$ ions; factually, the green luminescence increased gradually with progressive transformation from glasses to glass-ceramics. The authors explained that this trend is correlated with the growing efficiency of $Ho^{3+}$ and $Yb^{3+}$ migration inside the $CaF_2$ nanocrystal lattice, parallelly with an increase in the heat-treatment temperature from 650 to 725 °C; indeed, due to lower phonon energy inside the $CaF_2$ phase ($h\omega \approx 495$ cm$^{-1}$), the non-radiative relaxation from the ($^5S_2$,$^5F_4$) states is reduced. Similar correlations can also be found based on the analysis of photoluminescence (PL) results shown in the available literature for various types of optical hosts doped with $Ho^{3+}$ ions.[1,7,16,32] Thus, the modification in phonon energies around $Ho^{3+}$ ions may significantly affect their resultant photoluminescence properties. Those peculiarities may be involved in the appropriate tuning of the emission for dedicated applications in optoelectronics.

In this paper, we synthesized and characterized a series of $Ho^{3+}$-doped oxyfluoride nano-glass-ceramics containing the $LaF_3$ nanophase. The GCs were fabricated by annealing amorphous silicate xerogels at selected temperatures, *i.e.*, 700 and 900 °C. The structural measurements of the fabricated sol–gel samples involved the registration of X-ray diffraction (XRD) patterns and transmission electron microscopy (TEM) images, and the photoluminescence characterization consisted in recording the excitation (PLE) and emission spectra (PL within VIS, NIR and MIR ranges) along with the decay lifetimes from the several excited states of $Ho^{3+}$ ions, *i.e.*, ($^5S_2$,$^5F_4$), $^5F_5$, $^5I_6$, and $^5I_7$. This work is intended to systematize the correlations between local phonon energy, and the population as well as relaxation dynamics from the individual excited levels of $Ho^{3+}$ ions. Although the optical spectroscopy of $Ho^{3+}$ ions in singly- or multi-doped glass-ceramics (fabricated by high-temperature melt-quenching followed by further annealing) has been described in several previously published papers,[3,13,31,33–39] in this work, we synthesized and characterized $Ho^{3+}$-doped nano-glass-ceramics fabricated by a sol–gel method. As far as we know, there are only a few published articles concentrated on the synthesis pathway and luminescence characterization of $Ho^{3+}$-doped sol–gel glass-ceramic materials, *i.e.*, $SiO_2$-$PbF_2$ triply-doped with $Tm^{3+}/Yb^{3+}/Ho^{3+}$[40] and $SiO_2$-$LaF_3$ co-doped with $Yb^{3+}/Ho^{3+}$;[41] hence – in our opinion – it seems to be justi-

fied and reasonable to perform additional studies in this matter.

## Experimental

The series of xerogels activated by $Ho^{3+}$ ions were prepared using the sol–gel synthesis described in our previous paper.[42] All reagents were taken from Sigma Aldrich Chemical Company. The subsequent chemical reactions of tetraethoxysilane (TEOS), *e.g.*, hydrolysis, condensation, and polycondensation, were performed in a solution of ethanol, deionized water, and acetic acid with a molar ratio equal to 1 : 4 : 10 : 0.5 (95 mol%). Simultaneously, the solutions of $La(CH_3COO)_3$ and $Ho(CH_3COO)_3$ in trifluoroacetic acid (TFA) and deionized water were added dropwise to the TEOS-based mixtures. The molar ratio of $TFA : La^{3+} : Ho^{3+}$ was set on $5 : (1 - x) : x$ (5 mol%), where $x$ = 0.003 ($GC1_x$), 0.006 ($GC2_x$), 0.012 ($GC3_x$), 0.03 ($GC4_x$), 0.06 ($GC5_x$), and 0.12 ($GC6_x$). The as-prepared sols were dried at 35 °C for several weeks to form slightly orange-colored ($Ho^{3+}$) rigid xerogels. Finally, the nano-glass-ceramic materials were fabricated during heat-treatment of as-prepared xerogels at 700 and 900 °C, and the samples were appropriately denoted in the text as $GC_{700}$ and $GC_{900}$.

The fabricated glass-ceramics were characterized by powder diffraction measurements using a PANalytical X'Pert Pro MD diffractometer, which utilized the $CuK_{\alpha 1}$ X-ray line with a Bragg–Brentano standard setup included with a Ge(111) Johansson monochromator in the incident beam. The scanning range was set from 20° to 80°, with a step size of 0.016°. The full pattern fitting procedure was carried out using HighScore Plus (PANalytical) software version 3.1. and the PDF5+ 2024 (ICDD) database. The transmission electron microscopy (TEM) observations were performed using a JEOL high resolution (HR-TEM) JEM 3010 microscope working at an accelerating voltage of 300 kV and equipped with a Gatan 2k × 2k Orius™ 833SC200D CCD camera and an Elite T Energy Dispersive Spectroscopy (EDS) silicon drift detector (SDD) from AMETEK EDAX. The sol–gel samples were suspended in isopropanol, and after ultrasonication for 10 minutes, the resulting materials were deposited on a copper grid coated with an amorphous carbon film standardized for TEM observations. Selected area electron diffraction (SAED) patterns were characterized using ElDyf software (version 2.1). The luminescence measurements were performed using a Photon Technology International (PTI) Quanta-Master 40 (QM40) UV/VIS steady state spectrofluorometer supplied with a tunable pulsed optical parametric oscillator (OPO) pumped with the third harmonic of a Nd:YAG laser. The laser system was coupled with a xenon lamp, a double 200 mm monochromator, a multimode UV/VIS PMT (R928, PTI Model 914) and a Hamamatsu detector (H10330B-75). The excitation and emission spectra were recorded with a resolution of 0.5 nm. The luminescence decay curves were recorded using a PTI ASOC-10 (USB-2500) oscilloscope with an accuracy of ±0.1 μs. All structural and optical measurements were carried out at room temperature.

## Results and discussion

### Structural characterization of $Ho^{3+}$-activated glass-ceramics

The characterization of prepared $Ho^{3+}$-doped sol–gel materials began from the structural measurements using the XRD technique, and the recorded diffractograms are collected in Fig. 1. For samples from both of the fabricated series, independent of the applied heat-treatment conditions (*i.e.*, 700 or 900 °C), the well-visible diffraction patterns consisted of a set of lines characteristic for the $LaF_3$ phase with trigonal symmetry (ICDD: 032-0483). The details from the Rietveld refinement, *i.e.*, average crystal size, lattice parameters, unit cell volume, and weighted profile (R(%)) for individual $Ho^{3+}$-doped sol–gel samples are presented in Table S1.†

The average crystallite size ($D$) for individual sol–gel samples was calculated based on the peak broadening using the Scherrer equation as follows:

$$D = \frac{K\lambda}{\beta \cos \theta}, \quad (1)$$

in which $\lambda$ is the wavelength of the X-ray beam, $\beta$ is the width of the peak, $\theta$ is the Bragg angle, and $K$ refers to the Scherrer constant. The calculations were performed with the assumption of a pseudo-Voigt profile. For the glass-ceramics from the $GC_{700}$ series, the resultant crystallite sizes hesitate from 6.48 nm ($GC1_{700}$) to 11.81 nm ($GC6_{700}$), while for samples from the $GC_{900}$ series, the average sizes fluctuate from 13.99 nm ($GC1_{900}$) to 25.06 nm ($GC3_{900}$). It should be noted that the recorded XRD lines for $GC2_{700}$ and $GC5_{700}$ samples

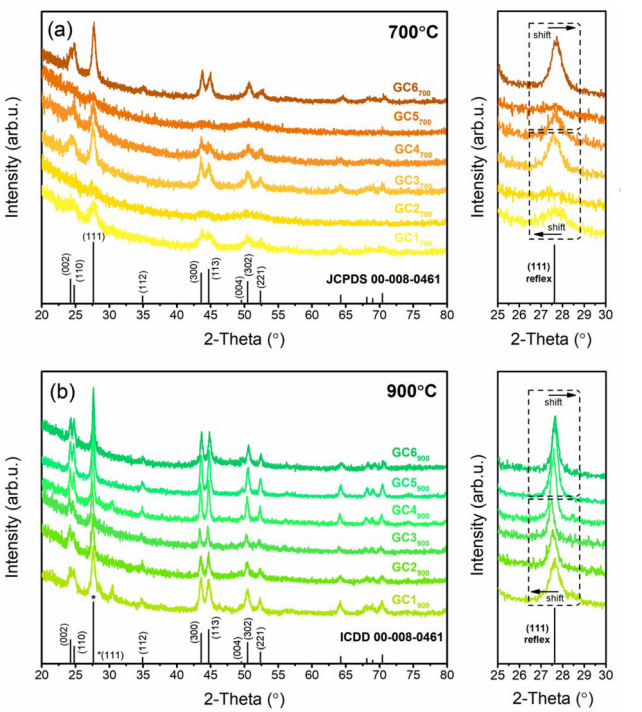


**Fig. 1** The XRD patterns of $Ho^{3+}$-doped sol–gel materials annealed at 700 °C (a) and 900 °C (b).

are not intense enough to estimate the average nanocrystal sizes.

Transmission electron microscopy (TEM) analysis was conducted for representative $GC6_{700}$ and $GC6_{900}$ samples (Fig. 2). The performed TEM investigations revealed the nanocrystalline nature of the materials; the micrographs recorded in the bright and dark fields apparently show that fabricated sol–gel glass-ceramics contain crystalline grains dispersed inside an amorphous host. The acquired selected area electron diffraction (SEAD) patterns were indexed using phase data sourced from the ICDD database with lattice parameter values obtained from XRD analysis. Based on microscopic images, it could be denoted that fluoride nanocrystals are dispersed more homogeneously within the amorphous silicate as the heat-treatment temperature was elevated from 700 °C to 900 °C. Additional energy-dispersive X-ray spectroscopy (EDS) and fast Fourier transform analysis (FFT) details are available in the ESI (Fig. S1†).

Another significant aspect according to the structural changes associated with an elevation in the heat-treatment temperature (700 °C → 900 °C) is the removal of residual OH groups from the silicate sol–gel host (characterized by high-oscillation energy, ~3500 $cm^{-1}$), as was previously demonstrated for analogous $SiO_2$-$LaF_3$ nano-glass-ceramics doped with $Pr^{3+}$ ions.[42] The elimination of OH groups also remarkably affects the photoluminescence behavior of the obtained materials, as was presented in the subsequent sections of this paper.

## Optical properties of fabricated sol–gel samples

**Emission spectra of $Ho^{3+}$-doped sol–gel samples in the VIS range.** The normalized photoluminescence emission spectra (PL) recorded inside the VIS region with the evaluated percentage contributions of individual luminescence bands are illustrated in Fig. 3. The PL lines were recorded upon excitation at $\lambda_{ex}$ = 450 nm, selected from the analysis of excitation spectra (Fig. S2†). The spectra clearly revealed the presence of characteristic luminescence bands of $Ho^{3+}$ ions, assigned to the following electronic transitions: $^3F_{2,3} \rightarrow {}^5I_8$ (480 nm), $(^5S_2,{}^5F_4) \rightarrow {}^5I_8$ (538 nm), $^5F_5 \rightarrow {}^5I_8$ (640 nm), and $(^5S_2,{}^5F_4) \rightarrow {}^5I_7$ (748 nm). It is quite interesting that the relative contribution of green ($(^5S_2,{}^5F_4) \rightarrow {}^5I_8$) and red ($^5F_5 \rightarrow {}^5I_8$) emission lines undergo progressive modifications as a result of both elevation in the heat-treatment temperature of as-prepared xerogels (1), as well as a change in the $Ho^{3+}$ concentration of the subsequent samples in the series (2). Finally, the resultant colors of the obtained emissions shift from the yellow-toned light region to green, as was presented in the Commission Internationale de l'Eclairage (CIE) chromaticity diagrams in Fig. S3†. Thus, to evaluate the mutual connotation in the population of the $(^5S_2,{}^5F_4)$ and the $^5F_5$ excited states, as well as to assess the relaxation dynamics

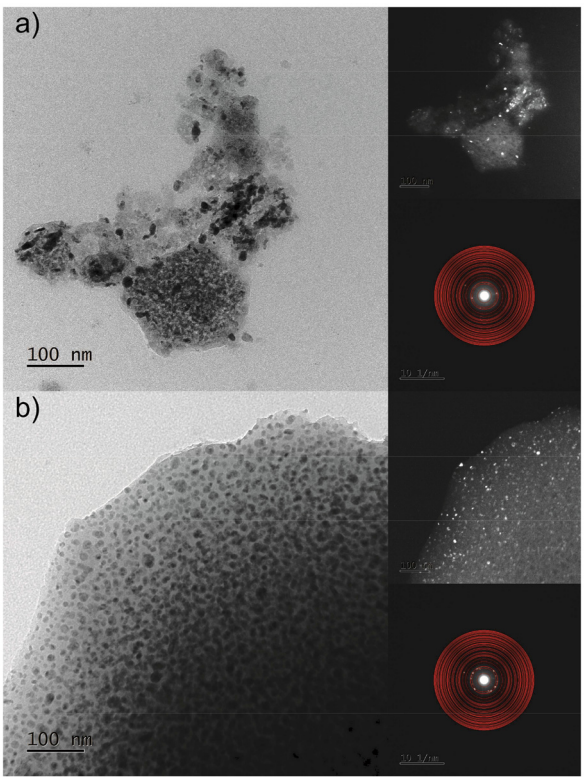


Fig. 2 TEM observations of the $GC6_{700}$ (a) and $GC6_{900}$ (b) samples. The right part of the columns presents corresponding dark field images and recorded SAED patterns. Red circles indicate theoretical Bragg positions.

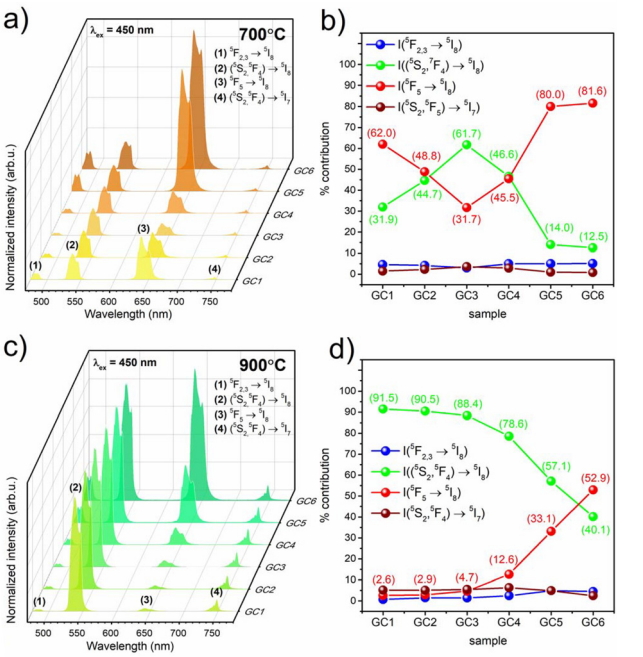


Fig. 3 The photoluminescence emission spectra (PL) of $Ho^{3+}$ ions recorded for fabricated sol–gel nano-glass-ceramics upon excitation at $\lambda_{ex}$ = 450 nm in the VIS range: presented as a function of increasing concentration of $Ho^{3+}$ ions (a and c), and the percentage involvement of individual luminescence bands (b and d). The data presented in Fig. (a and b) and (c and d) refer to GCs fabricated at 700 and 900 °C, respectively.

from the levels, the percentage involvement of each registered PL band ($\beta$) was determined (Table S2†).

The analysis of the percentage contribution values of individual PL bands clearly reveals that the relative share of green-toned luminescence (at $\lambda_{em}$ = 538 nm, according to the $(^5S_2,^5F_4) \rightarrow {}^5I_8$ transition of $Ho^{3+}$) is generally greater for the GCs fabricated by annealing carried out at 900 °C, compared to those heat-treated at 700 °C. Indeed, the calculated $\beta_{green}$ factors for subsequent samples from the $GC_{700}$ series modify as follows: 31.9% ($GC1_{700}$), 44.7% ($GC2_{700}$), 61.7% ($GC3_{700}$), 46.6% ($GC4_{700}$), 14.0% ($GC5_{700}$), and 12.5% ($GC6_{700}$); meanwhile for samples from the $GC_{900}$ series, $\beta_{green}$ exceed the following values: 91.5% ($GC1_{900}$), 90.5% ($GC2_{900}$), 88.4% ($GC3_{900}$), 78.6% ($GC4_{900}$), 57.1% ($GC5_{900}$), and 40.1% ($GC6_{900}$). The opposite trend was found for red emission (at $\lambda_{em}$ = 640 nm, assigned to the ${}^5F_5 \rightarrow {}^5I_8$ transition of $Ho^{3+}$); for samples from the $GC_{700}$ series, the $\beta_{red}$ factor changed from 62.0% ($GC1_{700}$), through 48.8% ($GC2_{700}$), 31.7% ($GC3_{700}$), 45.5% ($GC4_{700}$), 80.0% ($GC5_{700}$), up to 81.6% ($GC6_{700}$). The $\beta_{red}$ factor values are significantly reduced for glass-ceramics from the $GC_{900}$ series, which were estimated as: 2.6% ($GC1_{900}$), 2.9% ($GC2_{900}$), 4.7% ($GC3_{900}$), 16.6% ($GC4_{900}$), 33.1% ($GC5_{900}$) and 52.9% ($GC6_{900}$). Additionally, it is worth noting that regardless of the applied heat-treatment conditions, the percentage contribution of blue emission ($\lambda_{em}$ = 480 nm; ${}^3F_{2,3} \rightarrow {}^5I_8$ transition) and red/NIR luminescence ($\lambda_{em}$ = 748 nm; $(^5S_2,^5F_4) \rightarrow {}^5I_7$ transition) is negligible ($\beta_{blue}$ and $\beta_{red/NIR} \leq 5\%$) and does not change noticeably while the heat-treatment temperature was elevated from 700 to 900 °C.

Based on the above-mentioned mutual correlations in $\beta_{green}$ and $\beta_{red}$ values, it could be concluded that the population of the $(^5S_2,^5F_4)$ excited levels is greater (in comparison with the population of the lower-lying ${}^5F_5$ state) for samples heat-treated at 900 °C than for glass-ceramics obtained at 700 °C. For an illustration of the differences in the $\beta_{green}/\beta_{red}$ ratio of analogous samples from both of the prepared series, the PL spectra of representative $GC1_{700}$ and $GC1_{900}$ glass-ceramics were depicted (Fig. S4†). Such a relationship could be explained by considering the energy gap between the $(^5S_2,^5F_4)$ and the ${}^5F_5$ states, which are approximate equivalents to the oscillation energy of the OH group ($\Delta E \approx 3500$ cm$^{-1}$); hence, the presence of OH moieties in the immediate vicinity of $Ho^{3+}$ ions straightforwardly promotes the multiphonon relaxation (MPR) processes, resulting in a progressive depopulation of the $(^5S_2,^5F_4)$ levels with simultaneous pumping of the ${}^5F_5$ state. Taking into account that $\beta_{red}$ values are generally higher for samples from the $GC_{700}$ series, it could be assumed that the residual OH groups significantly affect the population of the lower-lying ${}^5F_5$ excited state of this part of $Ho^{3+}$ ions, which remained inside the silicate sol–gel host (even though we expect that part of $Ho^{3+}$ ions migrated into the crystallized $LaF_3$ nanophase). Furthermore, the dominant contribution of the $\beta_{green}$ factor for samples from the $GC_{900}$ series clearly suggests that the MPR to the ${}^5F_5$ level is suppressed and the electrons occupy primarily the $(^5S_2,^5F_4)$ states; the denoted changes in $\beta_{green}$ and $\beta_{red}$ parameters with an elevation in heat-treatment temperature point to two simultaneous factors. The first is correlated with the efficient removal of residual OH groups from the silicate host; thus, $Ho^{3+}$ ions that remained in the silicate network are surrounded by $Q^n$ [$SiO_4$] tetrahedral units with a lower oscillation energy ($\hbar\omega \approx 1220$ cm$^{-1}$). The second of the above-mentioned factors is associated with more efficient migration of $Ho^{3+}$ into the $LaF_3$ crystal lattice with a particularly low phonon energy ($\hbar\omega \approx 350$ cm$^{-1}$), which significantly reduces the probability of MPR occurring. Those considerations could also be confirmed by the augmented PL intensity for samples heat-treated at 900 °C compared to glass-ceramics obtained at 700 °C, as was shown for the representative $GC1_{700}$ and $GC1_{900}$ samples in Fig. S4.† Based on the conclusions from the analysis of PL spectra, the dominant transitions for samples annealed both at 700 and 900 °C were presented in the energy level diagram for $Ho^{3+}$ ions in Fig. 4.

Another interesting correlation is associated with the modification in the mutual participation of $\beta_{green}$ and $\beta_{red}$ parameters as a function of progressively growing $Ho^{3+}$ concentration in subsequent samples from the both prepared series. In the case of the $GC_{700}$ series, the change in the $La^{3+}:Ho^{3+}$ molar ratio from 0.997 : 0.003 ($GC1_{700}$) to 0.988 : 0.012 ($GC3_{700}$) resulted in the increasing involvement of the $(^5S_2,^5F_4) \rightarrow {}^5I_8$ green emission; meanwhile, a further decrease in the $La^{3+}:Ho^{3+}$ molar ratio to 0.88 : 0.12 ($GC6_{700}$) favors the contribution of ${}^5F_5 \rightarrow {}^5I_8$ red luminescence. It is anticipated that the observed tendency in values of $\beta_{green}$ and $\beta_{red}$ factors for $GC1_{700}$–$GC3_{700}$ glass-ceramics is probably correlated with the slightly enhanced ability of $Ho^{3+}$ ions to be incorporated into precipitated $LaF_3$ nanocrystals (as the concentration of $Ho^{3+}$ progressively grows). However, unexpectedly, for $GC3_{700}$–$GC6_{700}$ the trend in $\beta_{green}$ and $\beta_{red}$ factor values assumed the opposite direction, and finally, the involvement of the $(^5S_2,^5F_4) \rightarrow {}^5I_8$ green luminescence noticeably decreased. Herein, it should be noted that the concentration quenching process ($CQ_{Ho}$) started to occur from the $GC3_{700}$ sample; thus, the observed mutual modifications in the correlation between $\beta_{green}$ and $\beta_{red}$ parameters seem to be strictly associated with relaxation dynamics from the individual $(^5S_2,^5F_4)$ and the ${}^5F_5$ excited levels. Indeed, the obtained results indicate that the relaxation dynamics (realized by, *i.e.*, CR mechanisms, resonance energy transfer (RET), *etc.*) from the $(^5S_2,^5F_4)$ levels are much faster than that from the ${}^5F_5$ state. Such differences are responsible for faster quenching of the $(^5S_2,^5F_4) \rightarrow {}^5I_8$ green luminescence line compared to the ${}^5F_5 \rightarrow {}^5I_8$ red emission, causing the involvement of the latter band on the overall PL spectra to grow as the $Ho^{3+}$ concentration increases in $GC3_{700}$–$GC6_{700}$ samples. Similarly, for the glass-ceramics fabricated at 900 °C, the $CQ_{Ho}$ process begins from the $GC1_{900}$ sample with the lowest $Ho^{3+}$ concentration in the series; thus, a progressive diminishment in the contribution of the $(^5S_2,^5F_4) \rightarrow {}^5I_8$ green emission was noted, conversely to the ${}^5F_5 \rightarrow {}^5I_8$ red luminescence, the percentage involvement of which undergoes augmentation. The observed modifications in the $\beta_{green}/\beta_{red}$ ratio are closely related to the relaxation dynamics from the $(^5S_2,^5F_4)$ and the ${}^5F_5$ excited states. Our assumptions about the relax-

 

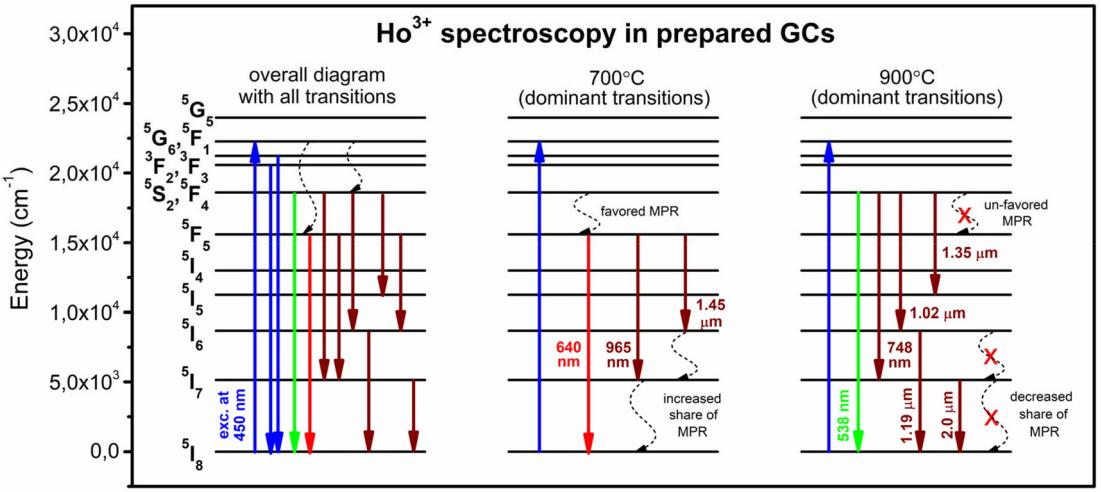


**Fig. 4** The energy level diagrams of $Ho^{3+}$ ions representing the dominant PL bands at 700 and 900 °C.

ation dynamics could also be confirmed by analysis of the $\tau(^5S_2,^5F_4)$ and the $\tau(^5F_5)$ decay times (see section Decay analysis of $Ho^{3+}$-doped GCs). The tunability in the color of emitted light, correlated color temperatures (CCTs), and color purities (CPs) were discussed and are depicted in the ESI (Table S3†).

**Emission spectra of $Ho^{3+}$-doped glass-ceramics in NIR and MIR regions.** The PL spectra recorded in the NIR range with an estimated contribution of each luminescence band for both series of $Ho^{3+}$-doped glass-ceramics are shown in Fig. 5. As a result, several emission bands assigned to the following transitions: $^5F_5 \rightarrow {}^5I_7$ (~0.97 μm), $(^5S_2,^5F_4) \rightarrow {}^5I_6$ (~1.02 μm), $^5I_6 \rightarrow {}^5I_8$ (~1.19 μm), $(^5S_2,^5F_4) \rightarrow {}^5I_5$ (~1.35 μm), and $^5F_5 \rightarrow {}^5I_6$ (~1.45 μm), were registered. Additionally, in the farther-located MIR region (also shown in Fig. 5), another luminescence band with a maximum located near ~2.0 μm (corresponding to the $^5I_7 \rightarrow {}^5I_8$ electronic transition) was recorded. It was observed that the intensities of PL bands inside the NIR region for nano-glass-ceramics fabricated at 700 °C overall increase for $GC1_{700}$–$GC3_{700}$ samples, but for $GC4_{700}$–$GC6_{700}$ glass-ceramics, the recorded intensity diminishes. For samples from the series fabricated at 900 °C, the NIR luminescence intensities decrease from the $GC2_{900}$ sample, clearly indicating that the $CQ_{Ho}$ process occurred parallelly with an increase in the concentration of $Ho^{3+}$ ions. In the case of emission recorded at ~2 μm (MIR region), the $CQ_{Ho}$ process starts to reveal from $GC4_{700}$ nano-glass-ceramics (for samples from $GC_{700}$ series), and from $GC2_{900}$ (for samples from $GC_{900}$ series, adequately).

Interestingly, it is well-visible that the PL profile in the NIR range is clearly determined by applied heat-treatment conditions; factually, the luminescence from the $^5F_5$ state is significantly suppressed for samples from the $GC_{900}$ series, as is also shown in Fig. S5† for the representative $GC4_x$ samples. Moreover, the PL intensity for glass-ceramics obtained at 900 °C is significantly greater compared to those registered for analogous samples from the $GC_{700}$ series. Therefore, to establish the mutual connotations in the preferable location of $Ho^{3+}$ ions (amorphous sol–gel framework or fluoride crystal environment), and in the population of the $(^5S_2,^5F_4)$ and the $^5F_5$ excited levels, the percentage involvement of individual NIR emission bands in the range of 950 nm to 1500 nm ($\beta$) was calculated, similar to that done for the VIS spectral range (Table S4†).

Based on the conclusions previously drawn, concerning the population of the $(^5S_2,^5F_4)$ and $^5F_5$ levels (from PL spectra recorded in the VIS spectral range), the percentage contributions of the following luminescence bands were also estimated: $^5F_5 \rightarrow {}^5I_7$ ($\beta_{NIR/0.97\ \mu m}$), $(^5S_2,^5F_4) \rightarrow {}^5I_6$ ($\beta_{NIR/1.02\ \mu m}$), $(^5S_2,^5F_4) \rightarrow {}^5I_5$ ($\beta_{NIR/1.35\ \mu m}$), and $^5F_5 \rightarrow {}^5I_6$ ($\beta_{NIR/1.45\ \mu m}$). For samples fabricated at 700 °C, the $\beta$ values changed in the $GC1_{700}$–$GC6_{700}$ sequence as follows: 16.0%, 9.5%, 5.0%, 7.7%, 23.7%, and 20.3% ($\beta_{NIR/0.97\ \mu m}$); 6.5%, 8.5%, 11.8%, 6.8%, and 1.5% ($\beta_{NIR/1.02\mu m}$); 24.3%, 25.4%, 29.5%, 18.5%, 11.4%, and 8% ($\beta_{NIR/1.35\ \mu m}$); 43.7%, 42.5%, 23.9%, 26.5%, 51.7%, and 63.1% ($\beta_{NIR/1.45\ \mu m}$). For samples heat-treated at 900 °C, $\beta_{NIR/0.97\ \mu m}$ values did not exceed 0.5%; $\beta_{NIR/1.02\ \mu m}$ values initially changed from 6.3% ($GC1_{900}$), through 3.8% ($GC2_{900}$), up to 7.4% ($GC3_{900}$), but then – for $GC4_{900}$–$GC6_{900}$ samples – drastically decreased to ≤0.5%. The $\beta_{NIR/1.35\ \mu m}$ values modify as follows: 14.6%, 9.0%, 19.3%, 11.0%, 1.7%, and 1.1%. The $\beta_{NIR/1.45\ \mu m}$ values do not exceed 2.1%. Herein, it could also be observed that the percentage involvement of PL bands associated with the electronic transitions from the $(^5S_2,^5F_4)$ levels, $\beta_{NIR/1.02\ \mu m}$ and $\beta_{NIR/1.35\ \mu m}$ gradually increases for samples heat-treated at 700 °C ($GC1_{700}$-$GC3_{700}$) with a nominal $La^{3+}:Ho^{3+}$ molar ratio modified from 0.997 : 0.003 to 0.988 : 0.012; meanwhile, the appropriate β parameters evaluated for transitions from the $^5F_5$ state (*i.e.*, $\beta_{NIR/0.97\ \mu m}$ and $\beta_{NIR/1.45\ \mu m}$) tend to decline. Thus, we could assume that such a correlation is probably associated with the slightly growing efficiency of $Ho^{3+}$ migration into the $LaF_3$ crystal lattice, simultaneously as the concentration of optically active ions increases

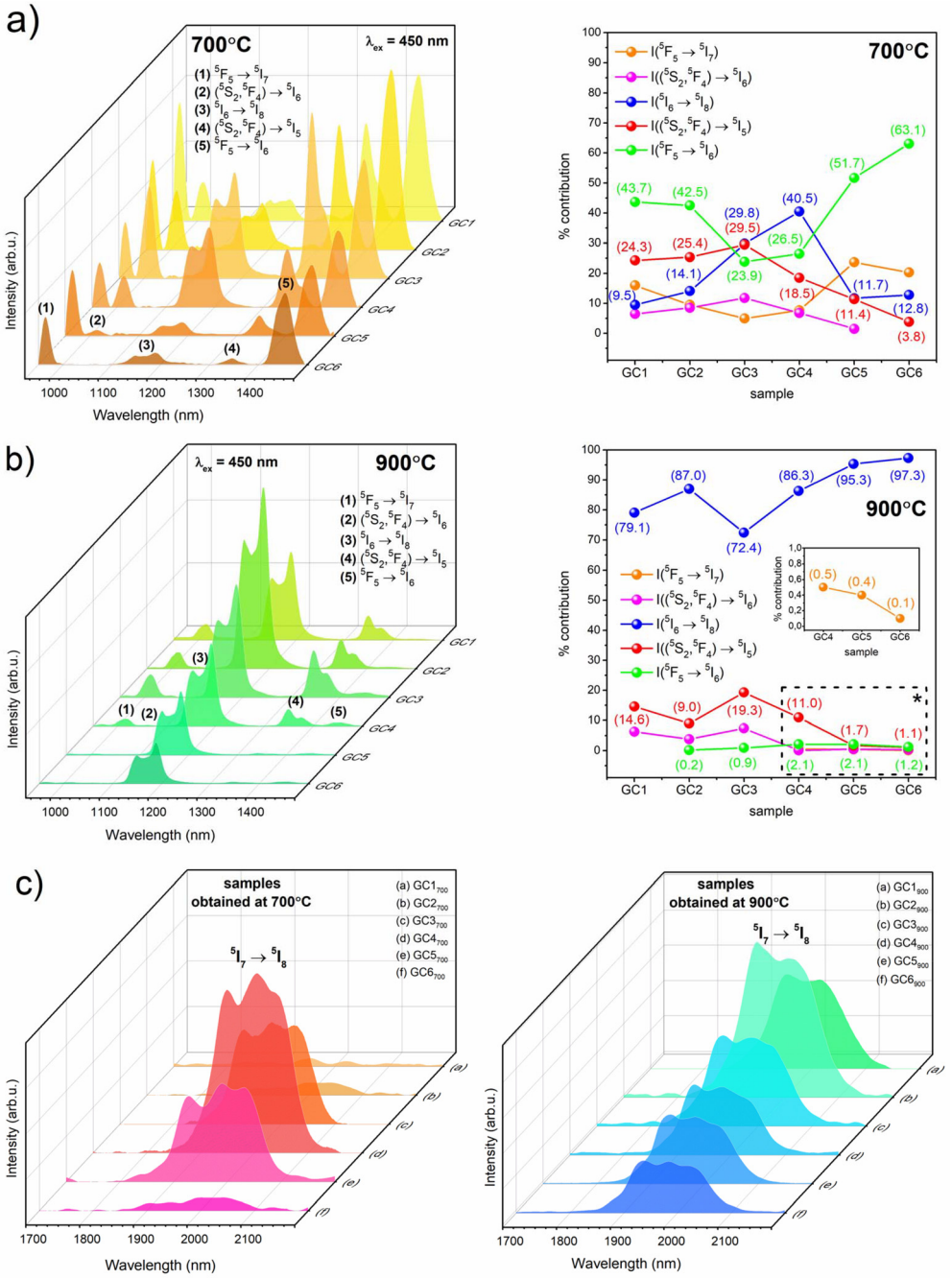


**Fig. 5** The PL spectra of $Ho^{3+}$ ions recorded for prepared GCs upon excitation at $\lambda_{ex}$ = 450 nm in the NIR range with the percentage contribution of individual emission bands (a and b), and the PL spectra registered in the MIR range for samples from the prepared $GC_{700}$ and $GC_{900}$ series (c).

(which may decrease the involvement of MPR from the upper-lying ($^5S_2$,$^5F_4$) levels to the lower-lying $^5F_5$ one). Upon exceeding the $La^{3+}$:$Ho^{3+}$ molar ratio beyond 0.988 : 0.012 ($GC3_{700}$), the trend in the percentage contribution starts to reverse, *i.e.*, $\beta_{NIR/1.02\ \mu m}$ and $\beta_{NIR/1.35\mu m}$ coefficients diminished, while the values of $\beta_{NIR/0.97\mu m}$ and $\beta_{NIR/1.45\ \mu m}$ parallelly increased. The indicated tendency originates in the $CQ_{Ho}$ process, which progressively occurs for $GC4_{700}$–$GC6_{700}$ glass-ceramics. Again, the non-radiative relaxation from the ($^5S_2$,$^5F_4$) levels proceeds more dynamically than from the $^5F_5$ state, which explains the mutual correlations in the intensities of the following PL bands: $^5F_5 \rightarrow {}^5I_7$, ($^5S_2$,$^5F_4$) → $^5I_6$, ($^5S_2$,$^5F_4$) → $^5I_5$, and $^5F_5 \rightarrow {}^5I_6$. Additionally, it is worth noting that the ($^5S_2$,$^5F_4$) → $^5I_6$ (~1.02 μm) and $^5F_5 \rightarrow {}^5I_6$ (~1.45 μm) electronic transitions favor the occupation of the $^5I_6$ state; hence, the $^5I_6 \rightarrow {}^5I_8$ (~1.19 μm) transition undergoes in the analyzed NIR spectral range. Considering the subsequent values of the $\beta_{NIR/1.19\mu m}$ coefficient for glass-ceramics fabricated at 700 °C: 9.5%

($GC1_{700}$), 14.1% ($GC2_{700}$), 29.8% ($GC3_{700}$), 40.5% ($GC4_{700}$), 11.7% ($GC5_{700}$), and 12.8% ($GC6_{700}$), it was assumed that for samples with the lowest $Ho^{3+}$ concentration, the relatively low probability for the $^5I_6 \rightarrow {}^5I_8$ transition to occur ($\leq$14.1%) should be related to the high impact of OH groups on the luminescence of $Ho^{3+}$ ions located inside the amorphous silicate sol–gel host. Indeed, since $Ho^{3+}$ ions are surrounded by functional groups or bonds with a high oscillation energy, like OH moieties, the non-radiative deactivation of the $^5I_6$ level could easily occur (the energy gap between the $^5I_6$ and the lower-lying $^5I_7$ state equals about ~3550 $cm^{-1}$), resulting in a relative low intensity of luminescence observed at ~1.19 μm. However, as the concentration of $Ho^{3+}$ ions increases, the probability of MPR from the $^5I_6$ state gradually decreases and the share of radiative $^5I_6 \rightarrow {}^5I_8$ emission enlarges. For the last samples from the series with the highest $Ho^{3+}$ concentration, *i.e.*, $GC5_{700}$ and $GC6_{700}$ (for which the $CQ_{Ho}$ occurs), another decrease in $\beta_{NIR/1.19\ \mu m}$ parameter values was denoted; it indicates a diminishing probability of radiative relaxation from the $^5I_6$ level. Moreover, it is also well-observed that the luminescence from the $^5I_6$ state quenched faster in comparison with the emission from the $^5F_5$ level; thus, we concluded that the non-radiative relaxation from the former excited level is more dynamic than from the latter one. The dominant transitions inside the IR region for the $GC_{700}$ series (and also for the $GC_{900}$ one) are presented in the energy level scheme in Fig. 4.

In the case of glass-ceramics from the $GC_{900}$ series, it is well-observed that the luminescence from the $^5F_5$ excited state has a little contribution to the overall recorded PL spectra, *i.e.*, $\beta_{NIR/0.97\ \mu m} \leq 0.5\%$ and $\beta_{NIR/1.45\ \mu m} \leq 2.1\%$. Factually, the population of the $^5F_5$ level for samples heat-treated at 900 °C is decreased (compared to samples from the $GC_{700}$ series) due to the more efficient location of $Ho^{3+}$ ions inside the fluoride crystal environment, where depopulation from the $(^5S_2,{}^5F_4)$ states to the lower-lying $^5F_5$ is restricted; additionally, the depopulation of the $^5F_5$ excited level also results from elimination of residual OH groups from the silicate sol–gel host. On the other hand, it is worth noting that the percentage contribution of emissions from the $(^5S_2,{}^5F_4)$ levels is also reduced in comparison with analogous glass-ceramics fabricated at 700 °C, and the resultant values of $\beta_{NIR/1.02\ \mu m}$ and $\beta_{NIR/1.35\mu m}$ parameters do not exceed 7.4% as well as 19.3%, respectively. The dominant involvement in PL spectra was attributed to the emission corresponding to the $^5I_6 \rightarrow {}^5I_8$ transition and the values of the $\beta_{NIR/1.19\mu m}$ parameter for individual samples were changed from 79.1% ($GC1_{900}$) to 97.3% ($GC6_{900}$). Such a domination of the $^5I_6 \rightarrow {}^5I_8$ transition could also be explained by the lowering of the local phonon energies around $Ho^{3+}$ ions, realized by more efficient incorporation of $Ho^{3+}$ inside the $LaF_3$ nanophase and removal of OH groups from the silicate network. Additionally, it was tentatively assumed that such a dominant contribution of the $^5I_6 \rightarrow {}^5I_8$ luminescence could probably be also associated with the CR process leading to the population of the $^5I_6$ state from the upper-lying $(^5S_2,{}^5F_4)$ by the involvement of the $\{(^5S_2,{}^5F_4) + {}^5I_8 \rightarrow {}^5I_6 + {}^5I_6\}$ mechanism.[43]

Similarly, as for the NIR spectral region, the PL spectra in the MIR range were also compared for representative samples, as is shown in Fig. S6.† It is well-visible that the luminescence near ~2 μm is more intense for nano-glass-ceramics fabricated at 900 °C, than for samples fabricated by controlled heat-treatment performed at 700 °C. Thus, the differences in the mutual band intensity are determined by two factors: efficient removal of residual OH groups from the immediate vicinity of $Ho^{3+}$ ions in the host, and their entry into the $LaF_3$ nanophase, which favors the radiative emission of the $^5I_7 \rightarrow {}^5I_8$ transition. In addition, the population of the $^5I_7$ excited state could also be associated with the CR process from the $(^5S_2,{}^5F_4)$ levels, realized by the following $\{(^5S_2,{}^5F_4) + {}^5I_8\} \rightarrow \{{}^5I_4 + {}^5I_7\}$ simultaneous electronic transitions.[43]

**Decay analysis of $Ho^{3+}$-doped GCs.** To further verify the photoluminescence behavior of fabricated $Ho^{3+}$-doped GC materials, the luminescence decay curves from the individual excited states, *i.e.*, $(^5S_2,{}^5F_4)$, $^5F_5$, $^5I_6$, and $^5I_7$ were evaluated. The registered curves are presented in Fig. 6 (for samples from the $GC_{700}$ series) and Fig. 7 (for glass-ceramics from the $GC_{900}$ series). The decay profiles follow the second-order exponential nature; therefore, the average lifetimes were calculated using the equation given below:

$$\tau_{avg} = \frac{A_1\tau_1^2 + A_2\tau_2^2}{A_1\tau_1 + A_2\tau_2}, \quad (2)$$

in which $A_1$ and $A_2$ are the residual weighting factors, and $\tau_1$ and $\tau_2$ are the fast and slow decay components, respectively. It could be observed that for $GC1_{700}$–$GC3_{700}$ glass-ceramic samples, the evaluated lifetimes – independent of the considered excited level of $Ho^{3+}$ ions – undergo gradual prolongation, while after exceeding the critical concentration of $Ho^{3+}$, a successive shortening in decay times was denoted ($GC4_{700}$–$GC6_{700}$). The identified progressive reduction in luminescence lifetimes is strictly associated with $CQ_{Ho}$. It is well-observable that among the evaluated lifetimes for the samples from the $GC_{700}$ series, *i.e.*, $\tau(^5S_2,{}^5F_4)$, $\tau(^5F_5)$, $\tau(^5I_6)$, and $\tau(^5I_7)$, the longest values were denoted for the $^5I_7$ excited level (with $\tau(^5I_7) = 1.5$ ms for the $GC3_{700}$ sample). Based on the available literature data (Table S5†), the estimated $\tau(^5I_7)$ lifetimes are very close to those determined for sol–gel silica glasses, as was presented in the previous work.[44] It should be noted that for ceramics, *e.g.*, $CaF_2:Ho^{3+}$ (in which optically active $Ho^{3+}$ ions are efficiently incorporated into the fluoride crystal lattice with a low-oscillation energy), the resultant lifetimes are much elongated, even to $\tau(^5I_7) \approx 30$ ms.[45] Thus, it could be justified that according to the fabricated glass-ceramics from the $GC_{700}$ series, $Ho^{3+}$ ions are mostly located inside the amorphous silicate sol–gel host; meanwhile, the minor part of accessible $Ho^{3+}$ is incorporated inside the $LaF_3$ nanocrystal fraction. These assumptions are consistent with the analysis of PL spectra, inside both the VIS and the NIR ranges (Fig. 3 and 5), which indicates that for samples from the $GC_{700}$ series, the population of the lower-lying $^5F_5$ excited level (typical of high-oscillation environments) is more efficient in comparison with

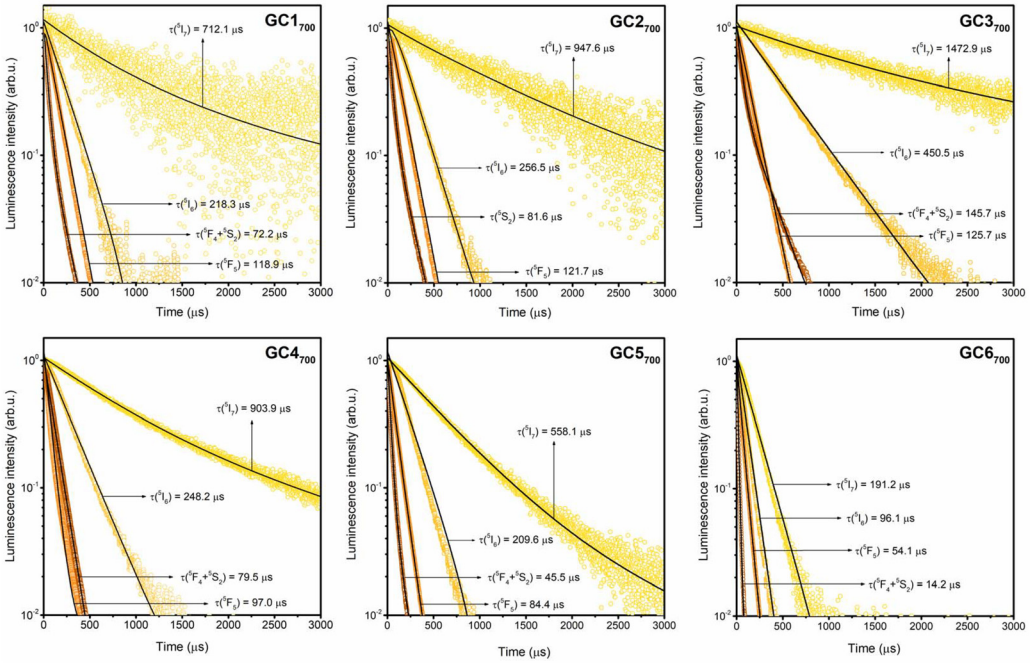


**Fig. 6** Luminescence decay curves for the individual excited states, *i.e.*, ($^5S_2$ + $^5F_4$), $^5F_5$, $^5I_6$, and $^5I_7$ of $Ho^{3+}$ in the prepared glass-ceramics from the series heat-treated at 700 °C.

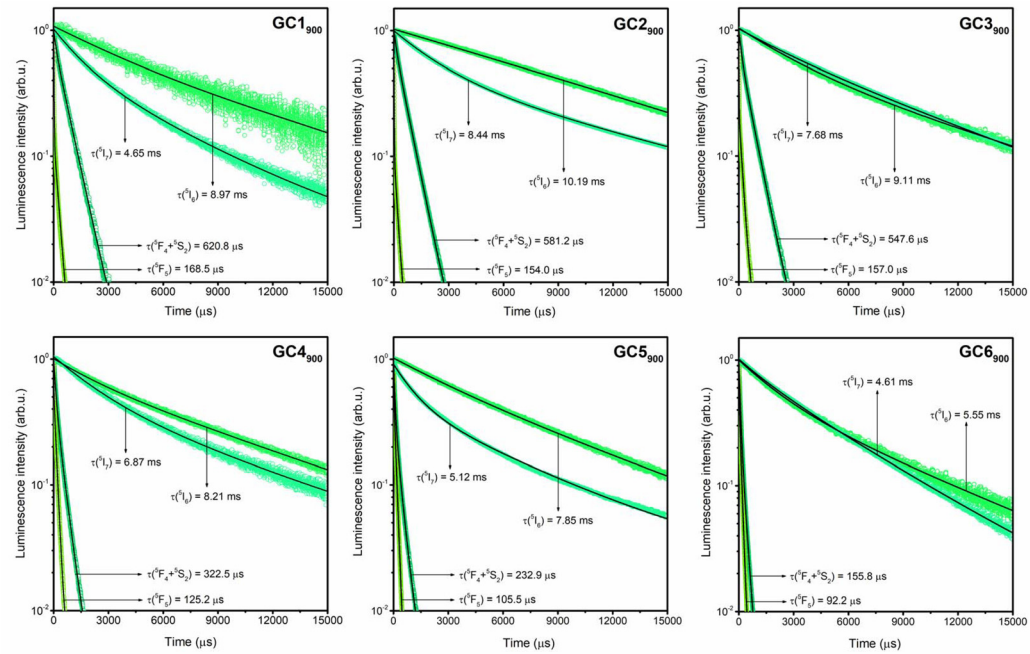


**Fig. 7** Luminescence decay curves for the individual excited states, *i.e.*, ($^5S_2$ + $^5F_4$), $^5F_5$, $^5I_6$, and $^5I_7$ of $Ho^{3+}$ in the fabricated sol–gel glass-ceramics from the series annealed at 900 °C.

analogous samples from the $GC_{900}$ series; similarly, the population of the upper-lying ($^5S_2$,$^5F_4$) states is less efficient for the $GC_{700}$ nano-glass-ceramics in comparison with samples fabricated at 900 °C. Hence, in the case of glass-ceramics annealed at 700 °C, the major part of $Ho^{3+}$ ions are probably located inside the high-phonon energy environment with residual OH groups, favoring the relaxation realized by the ($^5S_2$,$^5F_4$) → $^5F_5$ non-radiative MPR channel.

To evaluate the impact of $CQ_{Ho}$ on luminescence in the studied glass-ceramic samples, the efficiencies of the process were calculated based on the below equation:

$$\eta_{CQ} = \left(1 - \frac{\tau GCx}{\tau GC_{ref}}\right) \times 100\%, \quad (3)$$

where $\tau GCx$ refers to the lifetime of the appropriate excited state for the selected sample, while $\tau GC_{ref}$ corresponds to the longest decay time of the same excited level evaluated in the series (the reference sample for the series heat-treated at 700 °C is $GC3_{700}$; in the case of materials fabricated by annealing at 900 °C, the reference samples are $GC1_{900}$ (according to the lifetimes from the $(^5S_2,^5F_4)$ and $^5F_5$ excited levels) and $GC2_{900}$ (lifetimes from the $^5I_6$ and the $^5I_7$ states)). The obtained results for each of the excited states of $Ho^{3+}$ in glass-ceramics heat-treated at 700 °C are graphically demonstrated in Fig. S7.† By analyzing the decay lifetimes for the $(^5S_2,^5F_4)$ and the $^5F_5$ levels, it could be stated that $\eta_{CQ}(^5S_2,^5F_4)$ for the subsequent samples increases in the following order: 45.4% ($GC4_{700}$), 68.8% ($GC5_{700}$), and 90.2% ($GC6_{700}$), while $\eta_{CQ}(^5F_5)$ increases as follows: 22.8% ($GC4_{700}$), 32.8% ($GC5_{700}$) and 57.0% ($GC6_{700}$). The performed calculations clearly suggest that $\eta_{CQ}$ reached greater values for the $(^5S_2,^5F_4)$ levels compared to the lower-lying $^5F_5$ state, and therefore, the dynamics of the non-radiative relaxation from the former progresses faster with a gradual increase of the $Ho^{3+}$ concentration in the subsequent samples from the series. The observed differences in $\eta_{CQ}$ values for these two excited levels explain why the $\beta_{red}$ coefficients increase (from 31.7% ($GC3_{700}$) to 81.6% ($GC6_{700}$)), but $\beta_{green}$ coefficients parallelly diminish (from 61.7% ($GC3_{700}$) to 12.5% ($GC6_{700}$)) with the growing $Ho^{3+}$ concentration. In addition, the calculations of $\eta_{CQ}(^5I_6)$ were also performed, and the resultant values were estimated as: 44.9% ($GC4_{700}$), 53.5% ($GC5_{700}$), and 78.7% ($GC6_{700}$). Based on the previously performed analysis of the individual $\beta_{NIR}$ coefficients, it was stated that the luminescence quenching from the $^5I_6$ level (but also from the $(^5S_2,^5F_4)$ states) is faster compared to the quenching from the $^5F_5$ excited state; the same conclusion could be drawn from the analysis of calculated $\eta_{CQ}(^5I_6)$ and $\eta_{CQ}(^5F_5)$ efficiencies. Finally, the evaluated values of $\eta_{CQ}(^5I_7)$ changed as follows: 38.6% ($GC4_{700}$), 62.1% ($GC5_{700}$), and 87.0% ($GC6_{700}$). Thus, it could be stated that emission from the $^5I_7$ state also quenched faster than from the $^5F_5$ level; generally, the concentration quenching efficiencies decrease in the following order: $(^5S_2,^5F_4) > {}^5I_7 > {}^5I_6 > {}^5F_5$.

The further analysis of the obtained results involved the luminescence decay times for glass-ceramics from the $GC_{900}$ series. Hence, it could be observed that the gradual shortening in the decay times is achieved from $GC1_{900}$ (for $\tau(^5S_2,^5F_4)$ and $\tau(^5F_5)$) or from the $GC2_{900}$ sample for ($\tau(^5I_6)$ and $\tau(^5I_7)$). The progressive shortening in luminescence lifetimes is obviously correlated with the $CQ_{Ho}$ process; for $GC_{900}$ samples, the $CQ_{Ho}$ process begins from samples with lower $Ho^{3+}$ concentrations compared with glass ceramics fabricated at 700 °C. The longest lifetimes (in the millisecond range) were evaluated for the $^5I_6$ level (up to 10.19 ms for the $GC2_{900}$ sample) and the $^5I_7$ one (up to 8.44 ms for the same sample) in comparison with the decay times estimated for the $(^5S_2,^5F_4)$ and $^5F_5$ excited states (in the microsecond range). Moreover, regardless of the considered excited level, the determined lifetimes are prolonged for nano-glass-ceramic samples from the $GC_{900}$ series, compared to those evaluated for samples annealed at 700 °C (it is particularly noticeable for $\tau(^5I_6)$ and $\tau(^5I_7)$). Those differences in luminescence lifetimes for glass ceramics from the $GC_{700}$ and $GC_{900}$ series are strictly correlated with changes in phonon energies in the local environment around $Ho^{3+}$ ions. These assumptions are in good correlation with our earlier expectations about the greater population of the $(^5S_2,^5F_4)$ and $^5I_6$ levels for the $GC_{900}$ samples than for the $GC_{700}$ glass-ceramics, and conversely – lower occupancy of the $^5F_5$ excited state for the $GC_{900}$ series than for the $GC_{700}$ samples. It should also be noted that estimated luminescence lifetimes, *i.e.*, $\tau(^5S_2,^5F_4)$, $\tau(^5F_5)$, and $\tau(^5I_6)$, for glass-ceramics annealed at 900 °C, are elongated in comparison with other glass-ceramics or ceramic materials described in the literature, as was demonstrated in Table S5.† Only the $\tau(^5I_7)$ lifetimes are comparable to those reported for ceramics, *e.g.*, $Y_2O_3$:$Ho^{3+}$ and $Y_3Al_5O_{12}$:$Ho^{3+}$,[24] $(Lu,Sc)_2O_3$:$Ho^{3+}$,[46] or $Y_3NbO_7$:$Ho^{3+}$.[47]

Similarly, as for the samples from the $GC_{700}$ series, the impact of the $CQ_{Ho}$ process on luminescence behavior was evaluated. The results are graphically illustrated in Fig. S8;† the $\eta_{CQ}(^5S_2,^5F_4)$ values were evaluated as 6.4% ($GC2_{900}$), 11.8% ($GC3_{900}$), 48.0% ($GC4_{900}$), 62.5% ($GC5_{900}$), and 74.9% ($GC6_{900}$). Subsequently, the $\eta_{CQ}(^5F_5)$ reached the following values: 8.6% ($GC2_{900}$), 6.8% ($GC3_{900}$), 25.7% ($GC4_{900}$), 37.4% ($GC5_{900}$), and 45.3% ($GC6_{900}$). It could be observed that similar to the samples from the $GC_{700}$ series, the $\eta_{CQ}(^5S_2,^5F_4)$ values increase faster with the growing $Ho^{3+}$ concentration than the $\eta_{CQ}(^5F_5)$ values. It means that the non-radiative relaxation dynamics from the $(^5S_2,^5F_4)$ levels is higher than from the $^5F_5$ excited state, and it explains the progressive diminishment in the $\beta_{green}$ values (from 91.5% ($GC1_{900}$) to 40.1% ($GC6_{900}$)) in comparison with the progressively growing $\beta_{red}$ parameter (from 2.6% ($GC1_{900}$) to 52.9% ($GC6_{900}$)). Hence, the increasing contribution of the $^5F_5 \rightarrow {}^5I_8$ PL line with the growing concentration of $Ho^{3+}$ (in comparison with the decreasing contribution of the $(^5S_2,^5F_4) \rightarrow {}^5I_8$ emission band) is also observed for samples from the $GC_{900}$ series with more efficiently incorporated $Ho^{3+}$ ions inside the fluoride crystal phase, than in the case of the $GC_{700}$ glass-ceramics. In addition, by analyzing the correlations in the mutual percentage contribution of the $(^5S_2,^5F_4) \rightarrow {}^5I_6/{}^5I_5$ and $^5I_6 \rightarrow {}^5I_8$ NIR luminescence bands, it could be assessed that the non-radiative relaxation from the $(^5S_2,^5F_4)$ excited states is more dynamic than from the lower-lying $^5I_6$ level, which was also justified by the calculations of the $\eta_{CQ}(^5I_6)$ values, which changed as follows: 10.6% ($GC3_{900}$), 19.4% ($GC4_{900}$), 23.0% ($GC5_{900}$), and 45.5% ($GC6_{900}$). Finally, the $\eta_{CQ}$ efficiencies were also calculated for the $^5I_7$ level, and the resultant values change in the following order: 9.0% ($GC3_{900}$), 18.6% ($GC4_{900}$), 39.3% ($GC5_{900}$) and 45.4% ($GC6_{900}$).

The values are lower than the calculated $\eta_{CQ}(^5S_2,^5F_4)$ efficiencies for analogous glass-ceramic samples with the same concentration of $Ho^{3+}$ ions. In this case, the concentration quenching efficiencies decrease in general in the following order: $(^5S_2,^5F_4) > {}^5F_5 \approx {}^5I_6 \approx {}^5I_7$.

## Conclusions

In this work, we have synthesized and characterized a series of sol–gel nano-glass-ceramics (GCs) containing a $LaF_3$ nanocrystal phase and activated by $Ho^{3+}$ ions. The prepared sol–gel GCs exhibit luminescence bands within the VIS, NIR, and MIR spectral ranges, which were assigned to the intra-configurational electronic transitions within the $4f^{10}$ manifold of $Ho^{3+}$, and the most prominent emission lines were assigned to the following ones: $(^5S_2,^5F_4) \rightarrow {}^5I_8$ (green), $^5F_5 \rightarrow {}^5I_8$ (red), $^5I_6 \rightarrow {}^5I_8$ (NIR, ~1.19 μm), and $^5I_7 \rightarrow {}^5I_8$ (MIR, ~2.0 μm). Based on the mutual intensities of the recorded PL bands, their percentage contributions ($\beta$) were assessed; for the VIS range, it was established that – in general – the relative contribution of the $^5F_5 \rightarrow {}^5I_8$ red emission band is greater for samples fabricated at 700 °C; however, the green emission ($(^5S_2,^5F_4) \rightarrow {}^5I_8$) dominates for samples annealed at 900 °C. It was concluded that the relative population of the $(^5S_2,^5F_4)$ and lower-lying $^5F_5$ states is strongly correlated with the phonon energy in the nearest proximity around $Ho^{3+}$ ions in the host and (un)involvement of the $(^5S_2,^5F_4) \rightarrow {}^5F_5$ MPR channel. Indeed, based on the correlations in $\beta_{red}$ and $\beta_{green}$ coefficients, it was stated that the residual OH groups with high-oscillation energy (from the silicate sol–gel host) affect the population of the $^5F_5$ level for GCs heat-treated at 700 °C. Simultaneously, their removal by temperature elevation to 900 °C and the more efficient entry of $Ho^{3+}$ ions into the $LaF_3$ nanocrystal lattice favor the suppression of the relaxation from the $(^5S_2,^5F_4)$ states. Additionally, the emission recorded in the NIR (~1.19 μm) and MIR (~2.0 μm) regions is enhanced for nano-glass-ceramics fabricated at 900 °C. Notably, it was proven that the relaxation dynamics decrease in the following order: $(^5S_2,^5F_4) > {}^5I_7 > {}^5I_6 > {}^5F_5$ for samples from the series fabricated at 700 °C, and as follows: $(^5S_2,^5F_4) > {}^5F_5 \approx {}^5I_6 \approx {}^5I_7$ for nano-glass-ceramics heat-treated at 900 °C. In summary, the prepared $Ho^{3+}$-doped GCs are able to emit green light with high color purity (CP) reaching even 98%, and generate long-lived NIR/MIR emissions at ~1.19 μm (up to $\tau(^5I_6)$ = 10.19 ms) and ~2.0 μm (up to $\tau(^5I_7)$ = 8.44 ms), which could predispose them for use in optoelectronic devices.

## Author contributions

N.P.: writing – original draft, supervision, methodology, formal analysis, investigation, conceptualization, and data curation. J. Ś.: investigation, review and editing. B.H. and M.Z.: investigation, formal analysis, data curation, review and editing. M.S. and W.A.P.: resources, review and editing.

## Data availability

The data that support the findings of this study have been included as part of the ESI† and are also available from the corresponding author upon reasonable request.

## Conflicts of interest

There are no conflicts to declare.

## Acknowledgements

The research activities are co-financed by the funds granted under the Research Excellence Initiative of the University of Silesia in Katowice.

## References

1 Y. Ye, Z. Tang, Z. Ji, H. Xiao, Y. Liu, Y. Qin, L. Liang, J. Qi and T. Lu, *Opt. Mater.*, 2021, **121**, 111643.
2 V. Reddy Prasad, S. Damodaraian and Y. C. Ratnakaram, *Opt. Mater.*, 2018, **78**, 63–71.
3 W.-J. Zhang, Q.-J. Chen, Q. Qian and Q.-Y. Zhang, *J. Am. Ceram. Soc.*, 2012, **95**, 663–669.
4 L. Gomes, V. Fortin, M. Bernier, R. Vallée, S. Poulain, M. Poulain and S. D. Jackson, *Opt. Mater.*, 2016, **60**, 618–626.
5 M. Rajesh, D. Siva Raju and T. Kanagasekaran, *Ceram. Int.*, 2024, **50**, 49200–49209.
6 M. Ravi Prakash, G. Neelima, V. K. Kummara, N. Ravi, C. S. Dwaraka Viswanath, T. Subba Rao and S. Mahaboob Jilani, *Opt. Mater.*, 2019, **94**, 436–443.
7 M. Venkateswarlu, S. Mahamuda, K. Swapna, M. V. V. K. S. Prasad, A. Srinivasa Rao, S. Shakya, A. Mohan Babu and G. Vijaya Prakash, *J. Lumin.*, 2015, **163**, 54–71.
8 P. Rekha Rani, M. Venkateswarlu, K. Swapna, S. Mahamuda, M. V. V. K. Srinivas Prasad and A. S. Rao, *Solid State Sci.*, 2020, **102**, 106175.
9 K. Mariselvam and J. Liu, *J. Solid State Chem.*, 2021, **293**, 121793.
10 Y. Liu, X. Qin, L. Gan, G. Zhou, S. Hu, Z. Wang, J. Jiang, T. Zhang and H. Chen, *Materials*, 2024, **17**, 402.
11 V. Singh, A. A. Bhat, A. R. Kadam, S. Saravanakumar, P. K. Tripathi, S. J. Dhoble and J. B. Joo, *J. Electron. Mater.*, 2024, **53**, 6384–6394.
12 V. Singh, A. A. Bhat, C. M. Mehare and S. J. Dhoble, *J. Electron. Mater.*, 2024, **53**, 4857–4868.
13 K. Sathya Moorthy, E. Sailatha, P. Muralimanohar, K. S. Nagaraja and C. Karnan, *Inorg. Chem. Commun.*, 2023, **153**, 110770.
14 S. Ji, Y. Song, Z. Wang, C. Shen, J. Lin, B. Xiao, Q. Feng, Q. Du, H. Xu and Z. Cai, *Nanophotonics*, 2022, **11**, 1603–1609.

 

15 Y. Li, W. Wang, X. Huang, H. Chen, Y. Pan and X. Wei, *J. Lumin.*, 2021, **238**, 118280.
16 S. A. Jupri, S. K. Ghoshal, M. F. Omar and N. N. Yusof, *J. Alloys Compd.*, 2018, **753**, 46–456.
17 A. S. Alqarni, R. Hussin, S. N. Alamri and S. K. Ghoshal, *Res. Phys.*, 2020, **17**, 103102.
18 V. dos Santos de Souza, F. J. Caixeta, K. de Oliveira Lima and R. R. Gonçalves, *J. Lumin.*, 2022, **248**, 118978.
19 B. J. Chen, L. F. Shen, E. Y. B. Pun and H. Lin, *Opt. Commun.*, 2011, **284**, 5705–5709.
20 X. Zhu, J. Zong, A. Miller, K. Wiersma, R. A. Norwood, N. S. Prasad, A. Chavez-Pirson and N. Peyghambarian, Proc. SPIE, Fiber Lasers X: Technology, System, and Applications, 2013, 8601, 86010Y.
21 S. Wang, C. Li, C. Yao, S. Jia, Z. Jia, G. Qin and W. Qin, *Opt. Mater.*, 2017, **64**, 421–426.
22 S. Mahamuda, K. Swapna, P. Packiyaraj, A. Srinivasa Rao and G. Vijaya Prakash, *Opt. Mater.*, 2013, **36**, 362–371.
23 M. Liu, J. Zhang, J. Zhang, Z. Zhang, G. Farrell, G. Brambilla, S. Wang and P. Wang, *J. Lumin.*, 2021, **238**, 118265.
24 P. Loiko, L. Basyrova, R. Maksimov, V. Shitor, M. Baranov, F. Starecki, X. Mateos and P. Camy, *J. Lumin.*, 2021, **240**, 118460.
25 Y. Liu, Q. Li, L. Meng, Q. Pang, Y. Wang, H. Yao and Q. Chen, *Opt. Mater.*, 2024, **154**, 115694.
26 L. Tao, Y. H. Tsang, B. Zhou, B. Richards and A. Jha, *J. Non-Cryst. Solids*, 2012, **358**, 1644–1648.
27 R. Cao, Y. Lu, Y. Tian, F. Huang, Y. Guo, S. Xu and J. Zhang, *Sci. Rep.*, 2016, **6**, 37873.
28 J. Pan, R. Xu, Y. Tian, K. Li, L. Hu and J. Zhang, *Opt. Mater.*, 2010, **32**, 1451–1455.
29 H. Ebendorff-Heidepriem, I. Szabó and Z. E. Rasztovits, *Opt. Mater.*, 2000, **14**, 127–136.
30 Q. Liu, Y. Tian, C. Wang, F. Huang, X. Jing, J. Zhang, X. Zhang and S. Xu, *Phys. Chem. Chem. Phys.*, 2017, **19**, 29833–29839.
31 P. Babu, U. R. Rodríguez-Mendoza, V. Lavín and R. Praveena, *Opt. Mater.*, 2024, **153**, 115609.
32 M. A. Marzouk, I. M. Elkashef and H. A. Elbatal, *Appl. Phys. A*, 2019, **125**, 97.
33 Y. Gao, Y. Hu, D. Zhou and J. Qiu, *J. Nanosci. Nanotechnol.*, 2016, **16**, 3744–3748.
34 P. Liu, C. Han, X. Zhang, X. Li, Y. Wan, H. Zhang and C. Su, *Ceram. Int.*, 2024, **50**, 31164–31172.
35 F. Lahoz, S. E. Hernández, N. E. Capuj and D. Navarro-Urrios, *Appl. Phys. Lett.*, 2007, **90**, 201117.
36 K. Driesen, V. K. Tikhomirov, C. Görller-Walrand, V. D. Rodriguez and A. B. Seddon, *Appl. Phys. Lett.*, 2006, **88**, 073111.
37 G. Zhang, H. Wang, S. Xu, F. Jia, H. Zhang and C. Su, *J. Non-Cryst. Solids*, 2023, **619**, 122567.
38 A. Santana-Alonso, A. C. Yanes, J. Méndez-Ramos and J. Del-Castillo, *Sci. Adv. Mater.*, 2013, **5**, 592–597.
39 S. Jiang, H. Guo, X. Wei, C. Duan and M. Yin, *J. Lumin.*, 2014, **152**, 195–198.
40 J. del-Castillo, A. C. Yanes, J. Méndez-Ramos, V. K. Tikhomirov, V. V. Moshchalkov and V. D. Rodríguez, *J. Sol-Gel Sci. Technol.*, 2010, **53**, 509–514.
41 J. J. Velázquez, A. C. Yanes, J. del Castillo, J. Méndez-Ramos and V. D. Rodríguez, *Phys. Status Solidi A*, 2007, **204**, 1762–1768.
42 N. Pawlik, T. Goryczka, M. Zubko, J. Śmiarowska and W. A. Pisarski, *Nanoscale*, 2024, **16**, 4249–4265.
43 N. Bednarska-Adam, M. Kuwik, E. Pietrasik, W. A. Pisarski, T. Goryczka, B. Macalik and J. Pisarska, *Materials*, 2022, **15**, 5263.
44 X. Wang, W. Xu, S. Wang, C. Yu, D. Chen and L. Hu, *J. Alloys Compd.*, 2016, **657**, 478–482.
45 Z. Wan, W. Li, B. Mei, Z. Liu and Y. Yang, *J. Lumin.*, 2020, **223**, 117188.
46 W. Jing, P. Loiko, J. M. Serres, Y. Wang, E. Kifle, E. Vilejshikova, M. Augiló, F. Díaz, U. Griebner, H. Huang, V. Petrov and X. Mateos, *J. Lumin.*, 2018, **203**, 145–151.
47 L. Cornet, S. Guene-Girard, J.-M. Heintz, R. Boulesteix, A. Maître and V. Jubera, *Opt. Mater.*, 2023, **144**, 114319.